Chapter 68
Navigation Technology Research on GNSS Loop Structure Aided by Acoustic MEMS IMU

Cheng Jiang, Hailing Wu, Wenhai Jiao, Wang Wen and Xiaowei Cui

Abstract In order to improve the reliability of MEMS IMU application and the accuracy of integration navigation in high jerk environment, an acoustic MEMS Gyro was researched, the result show that the planar IC structure can transform the angle velocity to frequency output, and has better jerk tolerance compare with the three-dimensional structure silicon micro gyroscope in theory. The GNSS loop structure aided by acoustic MEMS gyro and accelerometer was designed and principally simulated. The results show that GNSS Loop Structure Aided by Acoustic MEMS IMU has great practicability potential.

Keywords Ultra-tight integration · Acoustic MEMS gyro · SAW gyro · Loop aided

68.1 Introduction

Ultra-tight Integration of Micro Electronic Mechanical System (MEMS) Inertial Measurement Unit (IMU) and Global Navigation Satellite System (GNSS) is a hot topic in recent years. MEMS IMU's advantages are small volume, low cost and

C. Jiang (✉) · H. Wu · W. Jiao
Beijing Institute of Tracking and Telecommunications Technology, Beijing, China
e-mail: jiangchengjc@gmail.com

H. Wu
e-mail: wuhl@beidou.gov.cn

W. Jiao
e-mail: jiaowh@beidou.gov.cn

W. Wen
The Chinese Academy of Sciences Institute of Acoustics, Beijing, China

X. Cui
Department of Electronic Engineering, Tsinghua University, Beijing, China

J. Sun et al. (eds.), *China Satellite Navigation Conference (CSNC) 2013 Proceedings*, Lecture Notes in Electrical Engineering 243,
DOI: 10.1007/978-3-642-37398-5_68,

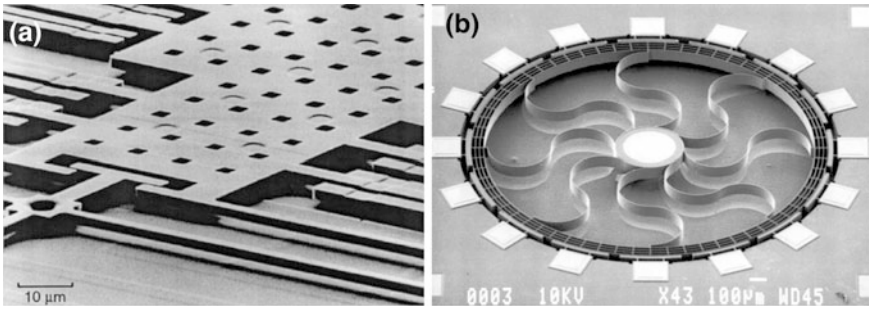

Fig. 68.1 ADXRS150 gyro capacitance measure unit (**a**) and MEMS four ring gyro (**b**)

high reliability, which can improve navigation survival ability and capacity of resisting disturbance when integrated with GNSS [1].

Traditional MEMS gyroscope use quartz or silicon material, the processing technology is Lithography and three-dimensional orientation of anisotropic etching, as a result, the sensors are in semi-suspended state, which are driven in resonant vibration by electro-circuit to sense Coriolis force. Two typical structures of silicon MEMS gyroscope are showed in Fig. 68.1.

Due to three dimensional structure and friableness of silicon-material, silicon MEMS gyroscope faces a challenge when using in cannonball which suffers from 20,000 g striking and strong oscillation. Even successful applications are reported in foreign publications, there is no application case in China. Meanwhile, output of silicon MEMS gyroscope is voltage or electric current, but not frequency, when integrated with code frequency and carrier frequency, additional errors and heavy calculation tasks are introduced.

A novel assistant GNSS tracking loop structure based on acoustic MEMS gyroscope is proposed in this article which can be applied to capturing and tracking GNSS signals. This structure is easier to realize and more efficiency.

68.2 The Principle and Experimental Results of SAW MEMS-IDT Gyroscope

The surface acoustic wave (SAW) based gyroscope provides a new way for angular rate detection with excellent inherent shock robustness, very larger dynamic testing range, small size, low cost, simplicity and long working life over currently available gyroscopes such as rotating wheel, fiber optic, laser, and micro machined gyroscopes [2]. It is very promising in real application of sports braking, electronic products and the guidance system for military.

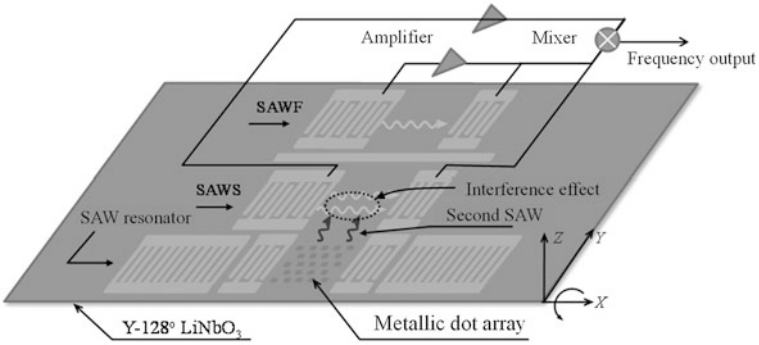

Fig. 68.2 The schematic of SAW gyroscope

68.2.1 Principle and Structure of SAW MEMS-IDT Gyroscope

In this paper, we propose a new design of SAW MEMS gyroscope with operation frequency of 80 MHz. Figure 68.2 shows the schematic diagram and working principle. It consists of a two-port SAW resonator with metallic dot array within the cavity, and two SAW oscillators structured by two delay lines in which one is used for a sensor element (SAWS) and the other is used for a reference element (SAWF). The details of the principle in our gyroscope system are as the following: A standing wave is generated on the two port resonator. Metallic dots at an antinode of the standing wave are vibrating in the normal direction (±z axis). When the gyroscope is subjected to an angular rotation, the induced Coriolis force acts on vibrating metallic dots, and it is proportional to the mass of the metallic dot (m), the vibrating velocity of the dot (v), and the rotational velocity of the substrate (Ω) ($F_{Coriolis} \sim 2\ mv \times \Omega$). Then, the Coriolis force generates a secondary SAW in the orthogonal direction of the primary standing wave (±y axis). The generated secondary SAW interferes with the Rayleigh SAW propagating in SAWS, causing a change in the acoustic velocity, and it induces a shift in the oscillator frequency. By measuring the mixed frequency difference between the sensor oscillator and the reference oscillator, the input rotation can be evaluated.

68.2.2 Sensitivity Evaluation of SAW MEMS-IDT Gyroscope

A new SAW gyroscope with 80 MHz based on standing wave mode was developed, and it consists of a two-port SAW resonator and two delay lines parelling to the resonator fabricated on a same 112°YX $LiTaO_3$ piezoelectric wafer. To improve the frequency stability of the oscillator, the single phase unidirectional transducers (SPUDTs) and combed transducers are utilized to structure the SAW

delay lines [3]. The fabrication procedure of the new SAW gyroscope is as fellows. Aluminum with thickness of 300 nm was deposited on the substrate by using thermal evaporator. Then, 1 μm thick photoresist (PR) was spin-coated, exposed, and developed for the resonator and two delay lines. Aluminum was wet-etched and PR was dissolved in acetone. Then, 10 μm thick PR was spin-coated, exposed, and developed for lift-off processing. The 300 nm thick gold dot array was deposited to obtain sufficient metallic mass. Finally, the PR was dissolved in acetone. The optical microscope and scanning electron microscopy (SEM) images of the fabricated SAW gyroscope are shown in Fig. 68.3. Individual components (resonator and SAW delay lines) were tested using the HP 8510 network analyzer without connecting to printed circuit board (PCB). RF power was applied, and the frequency response of each component was observed. First, the amplitude and phase response of S_{21} for SAW delay line were measured in the frequency domain under matched condition. As shown in Fig. 68.4a, low insertion loss of $\sim$7 dB was observed. Next, the frequency response of the two-port SAW resonator was characterized by the HP 8510 network analyzer. As shown in Fig. 68.4b, low insertion loss ($<$7 dB) was observed. A single steep resonant peak was observed in frequency bandwidth of the resonator due to the optimal spacing between the IDT and adjacent reflector.

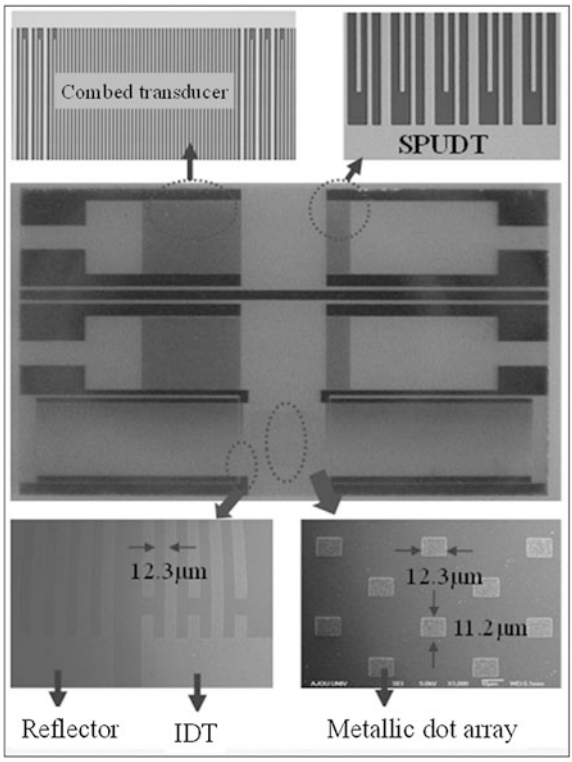

Fig. 68.3 SEM picture of the fabricated SAW gyroscope

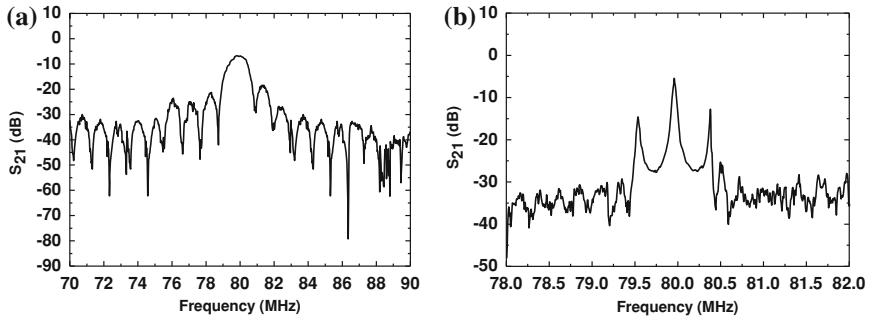

Fig. 68.4 Measured frequency response of **a** delay line and **b** resonator

Then, a voltage controller oscillator (VCO, KSV-5M075A, K.S.E Ltd.) was connected to the fabricated 80 MHz resonator to keep maintaining an 80 MHz resonant frequency in resonator by tuning the DC bias. The input and output transducers of the SAW delay line were connected by oscillator circuit, which is composed of amplifier with low gain, phase shifter, mixer, LC filter, and low pass filter (LPF). The output of two oscillators was mixed to reduce the influence of the thermal effect and provides low frequency signals in the KHz range. The output of the oscillator was monitored by a programmable frequency counter and the digital oscilloscope (GDS-2102).

The fabricated SAW gyroscope was mounted onto the PCB, and then the PCB was placed on the precision rate table (920CT) in vacuum chamber. The device was tested in vacuum. Constant temperature and humidity levels were maintained in the testing chamber during all the testing period to prevent any unwanted performance variations due to temperature and humidity changes. The input voltage of ±5 V was applied to the PCB when the rate table was not rotated. The output of the oscillator was monitored by the digital oscilloscope and programmable frequency counter.

As the rotation speed increases, the mixed oscillator frequency difference was increased as shown in Fig. 68.5 due to larger secondary wave interference to the SAWS induced by Coriolis force. The sensitivity of the SAW gyroscope with rotation in x-axis were measured in rate range of 0–200°/s as 119 Hz deg^{-1} s.

68.3 GNSS Loop Structure Based on Acoustic MEMS IMU

68.3.1 Physical Structure of Aided loop

Due to frequency outputs of acoustic MEMS IMU, frequency outputs can be applied to remove Doppler effect in carrier tracking loop directly, as shown in Fig. 68.6.

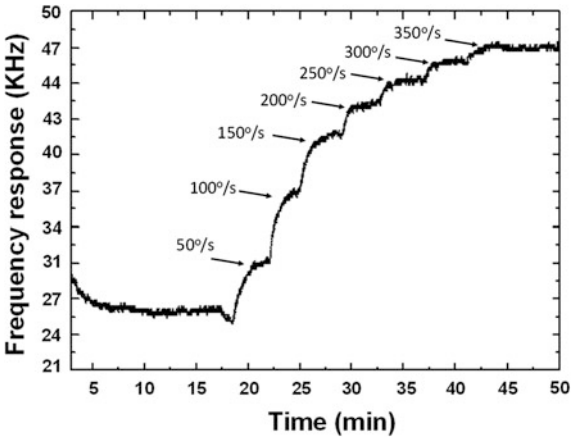

Fig. 68.5 Measured response of the fabricated SAW gyroscope

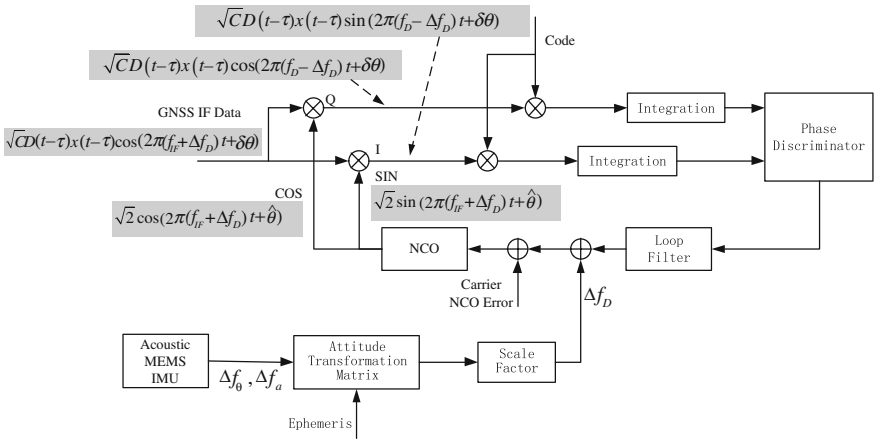

Fig. 68.6 Block diagram of Acoustic MEMS IMU aided GNSS integration

In Fig. 68.6, frequency outputs of acoustic MEMS IMU represent angular rate and acceleration of the GNSS receiver, multiplied by attitude transformation matrix and scale factor, Doppler frequency is made which represent relative velocity between satellites and the GNSS receiver.

After down-conversion, GNSS signal which sent to carrier tracking loop can expressed as:

$$\sqrt{C}D(t-\tau)x(t-\tau)\cos(2\pi(f_{IF}+f_D)t+\delta\theta) \tag{68.1}$$

where C stands for amplitude of signal, D is the navigation data, f_D is the true Doppler frequency, f_{IF} is intermediate frequency, τ is time-delay of the satellite signal, $\delta\theta$ is carrier phase.

Based on Doppler frequency measured by acoustic MEMS IMU, replica signal of SIN carrier and COS carrier can be expressed as:

$$\sqrt{2}\cos\left(2\pi(f_{IF}+\Delta f_D)t+\widehat{\theta}\right) \tag{68.2}$$

$$\sqrt{2}\sin\left(2\pi(f_{IF}+\Delta f_D)t+\widehat{\theta}\right) \tag{68.3}$$

Where Δf_D stands for Doppler frequency which produced by outputs of acoustic MEMS IMU and navigation data.

After mixing, time sample sequence of I path and Q path can be expressed as:

$$\sqrt{C}D(t-\tau)x(t-\tau)\cos(2\pi(f_D-\Delta f_D)t+\delta\theta) \tag{68.4}$$

$$\sqrt{C}D(t-\tau)x(t-\tau)\sin(2\pi(f_D-\Delta f_D)t+\delta\theta) \tag{68.5}$$

Even true Doppler can't be removed completely by Δf_D, but with Doppler aided from acoustic MEMS IMU, bandwidth of carrier tracking loop can be compressed effectively to improve navigation accuracy.

68.3.2 Calculation of Doppler Aided Frequency

Doppler frequency represents relative velocity between IMU and satellite. The Doppler frequency between the Kth satellite and IMU is:

$$\Delta f_D = e_k^T \cdot \frac{\Delta\left(V_{INS}-V_{SV,k}\right)}{\lambda_{L1}} \tag{68.6}$$

Which can be spread as [4]:

$$\Delta f_D = \frac{1}{\lambda_{B1}}\begin{bmatrix} e_{kx}\cdot\Delta(v_{INS,x}-v_{SV,xk})+e_{ky}\cdot\Delta(v_{INS,y}-v_{SV,yk}) \\ +e_{kz}\cdot\Delta(v_{INS,z}-v_{SV,zk}) \end{bmatrix} \tag{68.7}$$

Where λ_{B1} stands for wavelength of B, $e_k = [\,e_{kx} \quad e_{ky} \quad e_{kz}\,]^T$ is the line-of sight unit vectors from the MEMS IMU to the Kth satellite which can be calculated as:

$$e_k = \begin{bmatrix} e_{kx} \\ e_{ky} \\ e_{kz} \end{bmatrix} = \begin{bmatrix} \frac{\partial r_k}{\partial x} \\ \frac{\partial r_k}{\partial y} \\ \frac{\partial r_k}{\partial z} \end{bmatrix} = \begin{bmatrix} \frac{x-x_{s,k}}{r_k} \\ \frac{y-y_{s,k}}{r_k} \\ \frac{z-z_{s,k}}{r_k} \end{bmatrix} \tag{68.8}$$

In Eq. (68.8), (x, y, z) represent receiver position in ECEF, $\left(x_{s,k}, y_{s,k}, z_{s,k}\right)$ is the Kth satellite's position in ECEF, r_k is distance between the Kth satellite and receiver which can be expressed as:

$$r_k = \sqrt{(x - x_{s,k})^2 + (y - y_{s,k})^2 + (z - z_{s,k})^2} \tag{68.9}$$

In Eqs. (68.6) and (68.7), $V_{INS} = [\, v_{INS,x} \quad v_{INS,y} \quad v_{INS,z} \,]^T$ is velocity of IMU in ECEF which can be transformed from ENU Topocentric coordinate system to ECEF by multiplying transfer matrix R_l^e, $V_{INS} = R_l^e V^l$, R_l^e is [1]:

$$R_l^e = \begin{bmatrix} -\sin\lambda & -\sin\varphi\cos\lambda & \cos\varphi\cos\lambda \\ \cos\lambda & -\sin\varphi\sin\lambda & \cos\varphi\sin\lambda \\ 0 & \cos\varphi & \sin\varphi \end{bmatrix} \tag{68.10}$$

$V_{SV,k} = [\, v_{SV,xk} \quad v_{SV,yk} \quad v_{SV,zk} \,]^T$ is velocity of the Kth satellite in ECEF which can be calculated from ephemeris. Meanwhile, scale factor is defined by experiment fitting.

68.4 Simulation Verification

68.4.1 Simulation Trajectory Design

Design a coordinated turn trajectory of airplane, velocity of the airplane is 200 m/s, the trajectory is shown in Fig. 68.7. Suppose the bias stability of acoustic MEMS gyroscope is 150°/h, bias stability of acoustic MEMS accelerometer is 5 mg. Set 7 visual satellites, use intermediate frequency simulator to generate GNSS signal, pre-detection integration time is 20 ms, and use 2-order-FLL assisted 3-order-PLL carrier tracking loop structure, also code tracking loop is assisted by carrier tracking loop.

Without IMU aided, set FLL bandwidth to 20 Hz, set PLL bandwidth to 18 Hz, set DLL bandwidth to 2 Hz, with which generate the best performance [5, 6].

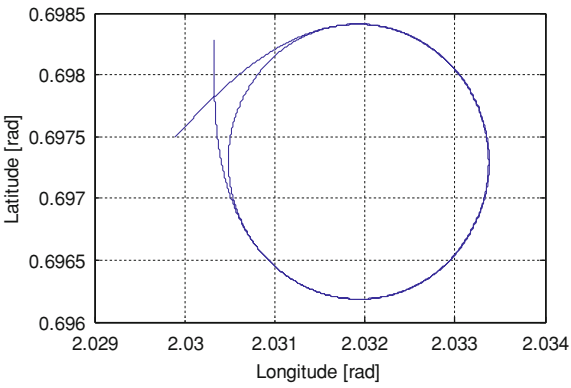

Fig. 68.7 Trajectory of the aircraft

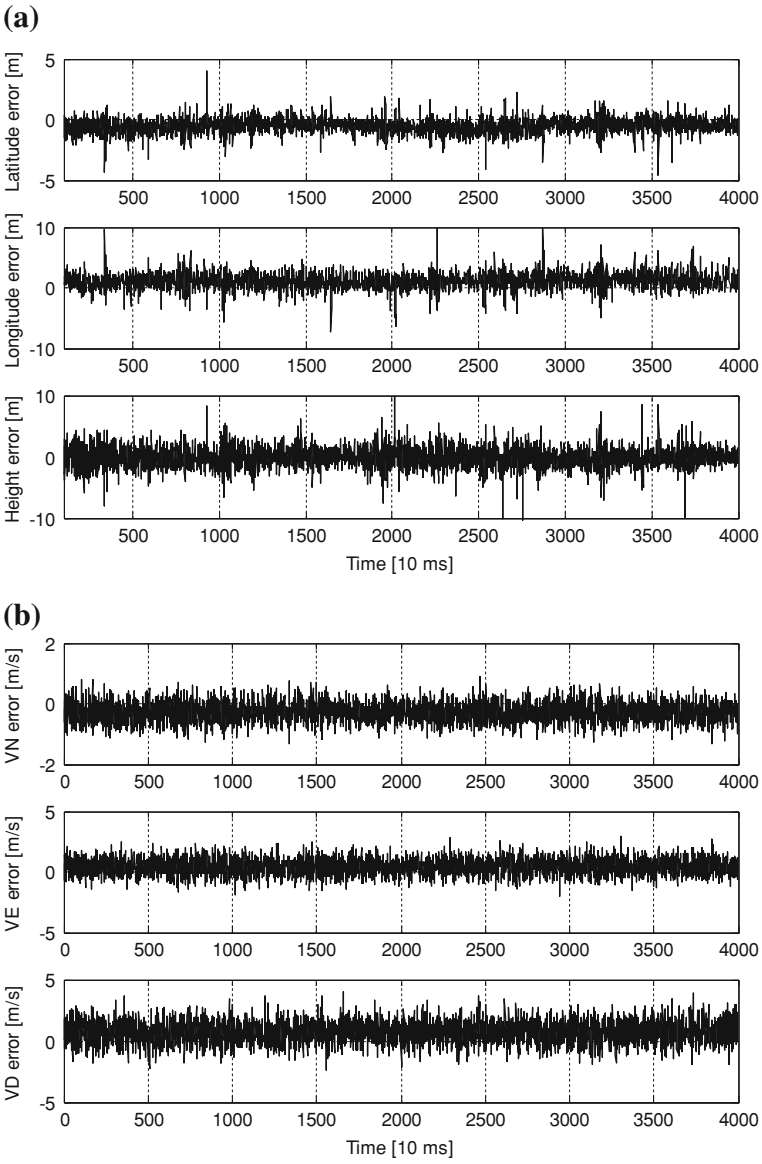

Fig. 68.8 Position errors (**a**) and Velocity errors (**b**) without IMU aided

With IMU aided, set FLL bandwidth to 10 Hz, set PLL bandwidth to 5 Hz, set DLL bandwidth to 1 Hz, under which the tracking loop can work stably.

During simulation, bandwidth of PLL could be adjusted below 5 Hz, tracking loop works steadily but tracking performance decreases.

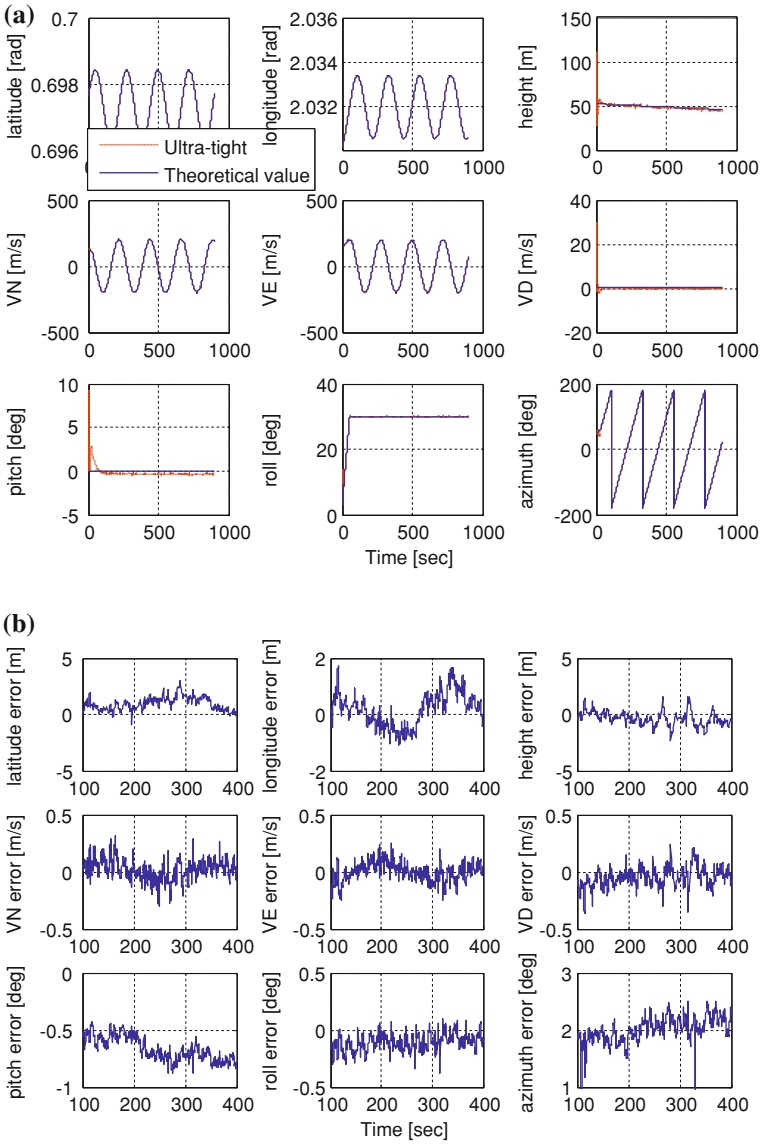

Fig. 68.9 Navigation results (**a**) and errors (**b**) with IMU aided

68.4.2 Simulation Result

Apply serial search capture method to re-capture GNSS signal. Simulation result shows that re-capture time is 10 s without IMU aided, 1 s with IMU aided.

Navigation performance is defined by comparing navigation result with ideal trajectory. As shown in Fig. 68.8, without IMU aided, position error is larger than 5 m, velocity error is larger than 1 m/s.

Figure 68.9 gives navigation performance with IMU aided, position error is less than 3 m, velocity error is less than 0.5 m/s, attitude error is less than 0.5°.

68.5 Conclusions

Firstly, principle and characteristic of a novel acoustic MEMS gyroscope are introduced. Then aided GNSS tracking loop structure is designed according to feature of acoustic MEMS IMU. Finally, simulation of ultra-tight integration method of acoustic MEMS IMU and GNSS is carried out. Simulation results show that compared with unaided method, PLL bandwidth can be compressed to 5 Hz, re-capture time change from 10 to 1 s, position error changes from 5 to 3 m, velocity error changes from 1 to 0.5 m/s, which indicate significant improvement.

References

1. Guo M, Lin S, Zhou B, Lv S, Liu G (2011) GPS/MINS tightly-coupled integrated navigation system. J Chin Inertial Technol
2. Lee SW et al (2007) A micro rate gyroscope based on the SAW gyroscopic effect, Micromech Microeng 17:2272
3. Wen SW (2011) Development of a new surface acoustic wave based gyroscope on a X-112o Y LiTaO3 substrate. Sensors 11(11):10894
4. Zhao S (2011) GNSS/INS integrated navigation: research on key technologies and working performance. PhD thesis, Tsinghua
5. Kaplan ED, Hegarty CJ (2006) Understanding GP—principles and applications, 2nd edn. Artech House, London
6. Parkinson BW, Spilker JJ (1996) Global positioning system: theory and applications. AIAA, Washington, DC